INL/RPT-22-69107-Revision-0

A physics-based model of cladding wastage layer formation rate

September 2022

Larry Kenneth Aagesen Jr, Chao Jiang

Changing the World's Energy Future

INL is a U.S. Department of Energy National Laboratory operated by Battelle Energy Alliance, LLC

INL/RPT-22-69107-Revision-0

A physics-based model of cladding wastage layer formation rate

Larry Kenneth Aagesen Jr, Chao Jiang

September 2022

Idaho National Laboratory
Idaho Falls, Idaho 83415

http://www.inl.gov

Prepared for the
U.S. Department of Energy
Under DOE Idaho Operations Office
Contract DE-AC07-05ID14517

INL/RPT-22-69107 Rev. 001

A physics-based model of cladding wastage layer formation rate

Technical Report

Larry K. Aagesen[1] and Chao Jiang[1]

[1]Idaho National Laboratory

INL is a U.S. Department of Energy National Laboratory
operated by Batelle Energy Alliance, LLC

A physics-based model of cladding wastage layer formation rate

Technical Report

Larry K. Aagesen[1] and Chao Jiang[1]

[1]Idaho National Laboratory

August 30, 2022

Idaho National Laboratory
Computational Mechanics and Materials Department
Idaho Falls, Idaho 83415

http://www.inl.gov

Prepared for the
U.S. Department of Energy
Office of Nuclear Energy
Under U.S. Department of Energy-Idaho Operations Office
Contract DE-AC07-05ID14517

Page intentionally left blank

Abstract

In this report, lower length scale simulations to inform an engineering-scale model of fuel-cladding chemical interaction (FCCI) conducted under the auspices of the Nuclear Energy Advanced Modeling and Simulation (NEAMS) program in FY22 are described. An overall strategy for the implementation of the BISON model is described, and the past and current lower length scale work on FCCI formation is put into the context of this overall strategy. Density functional theory and kinetic Monte Carlo simulations are used to determine the diffusion coefficient of neodymium in iron. Density functional theory calculations are also used to parameterize a parabolic approximation for the dependence of free energy on composition for the intermetallic compound $Fe_{17}Nd_2$. A phase-field model of the Fe-Nd system was developed that includes the random solid solution body-centered cubic phase and the intermetallic $Fe_{17}Nd_2$. The model was used to simulate growth of the intermetallic layer in a diffusion couple and the results were compared to experiment. The model's prediction of the parabolic growth constant is within 40 % of the experimental value. The model is also used to simulate the formation of a grain boundary attack layer that is observed in experiment. The simulations show enhanced Nd concentration along the grain boundaries, but do not clearly show formation of a $Fe_{17}Nd_2$ layer.

Page intentionally left blank

Acknowledgments

This report was authored by a contractor of the U.S. Government under contract DE-AC07-05ID14517. Accordingly, the U.S. Government retains a non-exclusive, royalty-free license to publish or reproduce the published form of this report, or allow others to do so, for U.S. Government purposes.

This research made use of the resources of the High Performance Computing Center at Idaho National Laboratory, which is supported by the DOE Office of Nuclear Energy and the Nuclear Science User Facilities under contract no. DE-AC07-05ID14517.

Page intentionally left blank

Contents

List of Figures

List of Tables

1. INTRODUCTION

The phenomenon of fuel-cladding chemical interaction (FCCI) has historically been one of the main performance limitations for U-(Pu)-Zr metallic fuel for nuclear reactors. The problem involves a complex set of chemical interactions between the fuel and the stainless steels typically used for cladding, including grades 316, D9, and HT9 [1]. Although FCCI results in microstructural changes in both the fuel and cladding sides of the interface, the most severe limitation to fuel performance arises from the formation of a brittle layer on the interior of the cladding surface, sometimes referred to as cladding wastage.

In spite of the limitations that FCCI and in particular cladding wastage places on fuel element performance, there remains a fairly limited understanding of the microstructure of the wastage layer. Experimental characterization of fuel elements irradiated in the Experimental Breeder Reactor-II (EBR-II) showed that the lanthanide elements Nd and Ce penetrated furthest into the cladding [2]. These lanthanides penetrated deeper into HT9 and D9 cladding than into 316. An intermetallic phase $(Fe,Cr,Si)_{17}(Nd,Ce)_2$, was observed to form, with Nd and Fe being the most prevalent species on each of the respective sublattices [2].

More recently, experimental characterization was performed on U-10Zr (wt. %) fuel with HT9 cladding irradiated in the Fast Flux Test Facility (FFTF) [3]. A region of the cladding with enhanced concentration of lanthanides along the cladding grain boundaries was observed that had not been seen previously in Ref. [2]. This region is labeled as Region B in Figure 1.1 [3]. It is possible that the $(Fe,Cr,Si)_{17}(Nd,Ce)_2$ phase has formed along these grain boundaries, although this has yet to be confirmed. In addition, a region of highly enhanced lanthanide concentration is observed as region C in Figure 1.1. This is the region that has been more typically associated with the FCCI phenomenon and will be referred to as the fully formed FCCI layer in this report. Multiple phases are present in this layer, and they have not all been conclusively identified, although it is believed that $(Fe,Cr,Si)_{17}(Nd,Ce)_2$ is one of them.

To allow fuel designers to better predict the effect of FCCI on fuel performance, an empirical model of cladding wastage layer formation has been implemented in the BISON fuel performance code. However, given that the model is purely empirical in nature, it cannot accurately predict FCCI formation outside of the conditions used to develop the model. This limits fuel designers as they explore novel reactor concepts. The empirical model is also not adaptable to different cladding materials. For these reasons, a physics-based, mechanistic model of FCCI is under development through the U. S. Department of Energy's Nuclear Energy Advanced Modeling and Simulation (NEAMS) program. Previous work has focused on the diffusion of lanthanides through the fuel. In this report, the focus is on diffusion of the most prevalent of the lanthanide species, neodymium (Nd), through the cladding, and the formation of the intermetallic compound. The organization of the report is as follows. In Chapter 2, the overall strategy for development

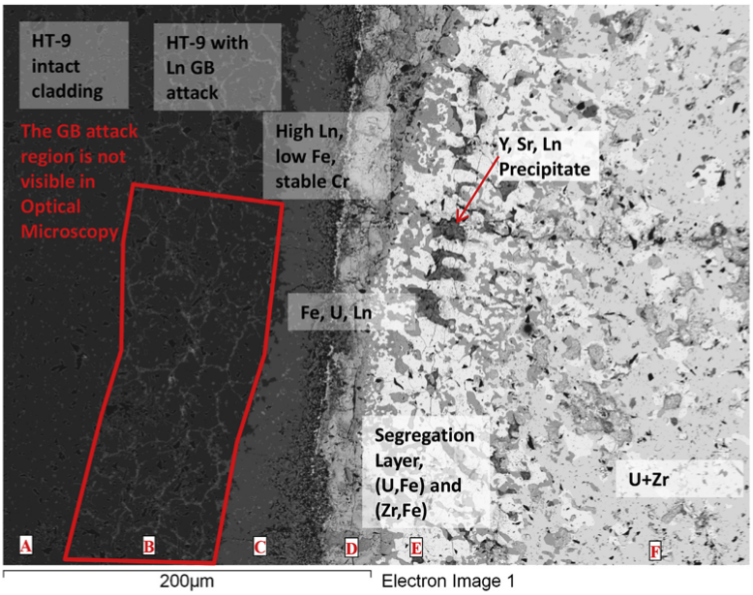

Figure 1.1. Microstructure of FCCI region of U-10Zr fuel with HT9 cladding, with cladding at left (Regions A, B, C) and fuel at right (Regions D, E, F) [3].

of a mechanistic model of FCCI in BISON is discussed, and past and current lower length scale simulations to develop and parameterize the model are put into the context of the overall FCCI model development. Future lower length scale needs to complete the model are also given. In Chapter 3, atomistic calculations are used to determine the diffusion coefficient of Nd atoms through the Fe matrix, along with other parameters needed to complete a phase-field model of the Fe-Nd system. The phase-field model is described in Chapter 4, including the formulation and parameterization. The model is used to simulate the growth of a uniform layer of $Fe_{17}Nd_2$ and compared to a diffusion couple experiment. The model is also tested for use in simulations of grain boundary attack as observed in Ref. [3]. Finally, in Chapter 5, conclusions are drawn, and outlook and recommendations for future work are given.

2. STRATEGY FOR BISON MODEL DEVELOPMENT

The purpose of this section is to describe the overall approach to developing a physics-based model of cladding wastage layer formation in BISON and to describe the lower-length-scale simulations that are needed to parameterize it. The initial focus of the BISON model development is on HT9 cladding.

The process of cladding wastage layer formation has been described to occur in five steps: 1) formation of lanthanides in the fuel; 2) transport of lanthanides to fuel pin edge; 3) swelling of the fuel until it contacts the cladding and cracking of the outer edge of the fuel pin; 4) transport of lanthanides through the sodium bonding layer to the cladding; and 5) diffusion of lanthanides into the cladding [1]. The cracking of the fuel in Step 3 is considered an important part of the process because prior to crack formation, a Zr "rind" is present at the edge of the fuel pin that forms an effective barrier to diffusion of lanthanides. The depth of the cracks is larger than the rind thickness, which allows lanthanides to diffuse out.

The strategy for BISON modeling of each step is described below, along with the lower-length-scale simulations needed to inform each step. The initial focus is on Nd, but a similar approach can be used for other lanthanide species.

- Step 1: formation of lanthanides in the fuel. The production rate of Nd can be calculated from the fission rate in the fuel pin times the fission yield of Nd. A nonlinear variable for Nd concentration will be added to the BISON model, and a source term for the production rate (using a BodyForce kernel) will be added in the fuel pin.

- Step 2: transport of lanthanides to fuel pin edge. Diffusion of the Nd through the fuel will be calculated using the temperature- and porosity-dependent effective diffusivity, which has been calculated using lower length scale simulations in Ref. [4, 5]. A BISON model will be created that implements the results of these studies as a material property. The model will incorporate the effects of sodium infiltration into the fuel by making use of an existing BISON variable that tracks the volume of sodium logging.

- Step 3: swelling of the fuel until it contacts the cladding and cracking of the outer edge of the fuel pin. Multiple swelling models for U-(Pu)-Zr fuel are currently available in BISON, as well as a contact detection algorithm. Prior to mechanical contact between the fuel and cladding, lanthanides will need to diffuse through the sodium bonding layer (Step 4); once the fuel comes into mechanical contact with the cladding, solid-state diffusion may allow transport of lanthanides directly. However, the presence of the Zr "rind" may prevent transport both before and after contact occurs. A mechanistic model of crack formation in the fuel pin is currently not available. Therefore, an approach similar to that employed in the current BISON model `MetallicFuelWastage` will be used, where a user-controlled burnup at which crack formation occurs is an input parameter to the model. Prior

to crack formation, a low-diffusivity region to give the effect of the rind will be placed at the edge of the fuel in the BISON material property for diffusivity; following crack formation, this low-diffusivity region will be removed.

- Step 4: transport of lanthanides through the sodium bonding layer to the cladding. The diffusion coefficient of lanthanides through liquid sodium will be taken from existing atomistic calculations from the literature [6].

- Step 5: diffusion of lanthanides into the cladding. A new material object will be created for BISON that will calculate the cladding wastage layer thickness as a function of time and lanthanide concentration at the edge of the fuel pin. Both the thickness of the GB attack region and the fully formed FCCI layer will be considered. The functions describing the growth rate for these regions will be determined using lower-length scale simulations. The phase-field model described in Chapter 4 has been developed as a basis to perform these calculations, informed by the atomistic simulations of Chapter 3. For the Fe-Nd binary system, the model has been shown to be able to predict the growth rate of the intermetallic phase $Fe_{17}Nd_2$ from a diffusion couple reasonably well. However, the morphology of the fully formed FCCI layer is more likely complex than a uniform $Fe_{17}Nd_2$ layer [3]. In future work, the binary model will be extended to include Cr and the effect on FCCI layer morphology will be determined. Phase-field simulations of layer growth will be performed, with time-varying lanthanide concentration from BISON simulations used as a boundary condition. A function of the form $T = Ct^{\alpha}$ will be fit based on the simulations for implementation in the BISON material, where α is expected to differ from 1/2 due to the time-varying boundary condition (BC), as opposed to the constant concentration BC that results in parabolic growth. Depending on the morphology when additional chemical constituents are added, 2D simulations may be required rather than 1D. A similar approach will be used to simulate the growth of the GB attack layer, with a representative grain structure for HT9 used as an input parameter to phase-field simulations. The analytical equations for the growth rate derived from these phase-field simulations will be implemented in the BISON model.

3. ATOMISTIC SIMULATIONS TO OBTAIN KINETIC AND THERMODYNAMIC PROPERTIES OF THE IRON-NEODYMIUM SYSTEM

A fundamental understanding of lanthanide transport in both metallic fuels and claddings is critical for multi-scale modeling of the fuel-cladding chemical interaction (FCCI) phenomenon. In a recent study [4], the diffusivity of Nd in α-U has been predicted using a combination of ab initio density functional theory (DFT) calculations and kinetic Monte Carlo (KMC) simulations. In this chapter, the same approach has been applied to study the diffusion of Nd in α-Fe with a body-centered cubic (bcc) crystal structure. The point defect structure of the $Fe_{17}Nd_2$ intermetallic compound in the Fe-Nd binary system has been further investigated by DFT. Results from the present lower length scale study will be used to inform mesoscale phase-field simulations of FCCI.

3.1 Point Defect Structure of $Fe_{17}Nd_2$

In the thermodynamic modeling of the Fe-Nd system [7], the $Fe_{17}Nd_2$ phase has been treated as a line compound with no homogeneity range. To obtain the effects of small deviation from stoichiometry on the formation energy of the $Fe_{17}Nd_2$ phase, we have performed DFT calculations to investigate its point defect structure. As illustrated in Figure 3.1, $Fe_{17}Nd_2$ has a complex trigonal crystal structure with space group R-3m [8]. In this structure, Fe atoms occupy $6c$, $9d$, $18f$, and $18h$ sites, while Nd atoms occupy $6c$ sites. Our DFT calculations show that Fe antisite (a Fe atom occupying a Nd_{6c} site) and Nd antisite (a Nd atom occupying a Fe_{6c} site) are the most stable defects in Nd-depleted and Nd-rich $Fe_{17}Nd_2$, respectively. The defective $Fe_{17}Nd_2$ structure is modeled by changing or removing a single atom in a 228-atom supercell. The details of DFT calculations can be found in Section 3.2.1. As shown in Figure 3.2, our DFT calculated formation energies of defective $Fe_{17}Nd_2$ can be accurately fitted using a parabolic function with a curvature of 441.3 eV/atom, or 4.26×10^7 J/mol.

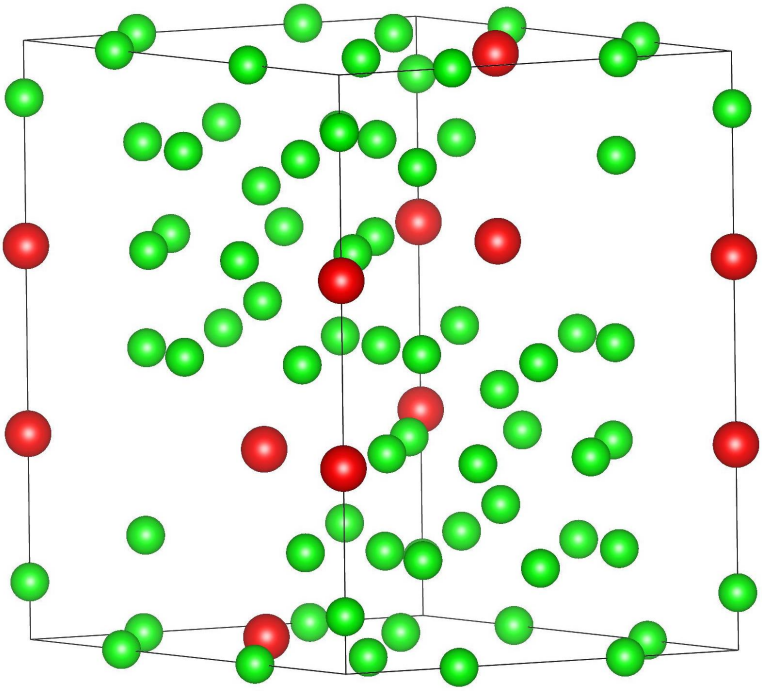

Figure 3.1. Crystal structure of $Fe_{17}Nd_2$. Green and red spheres represent Fe and Nd atoms, respectively.

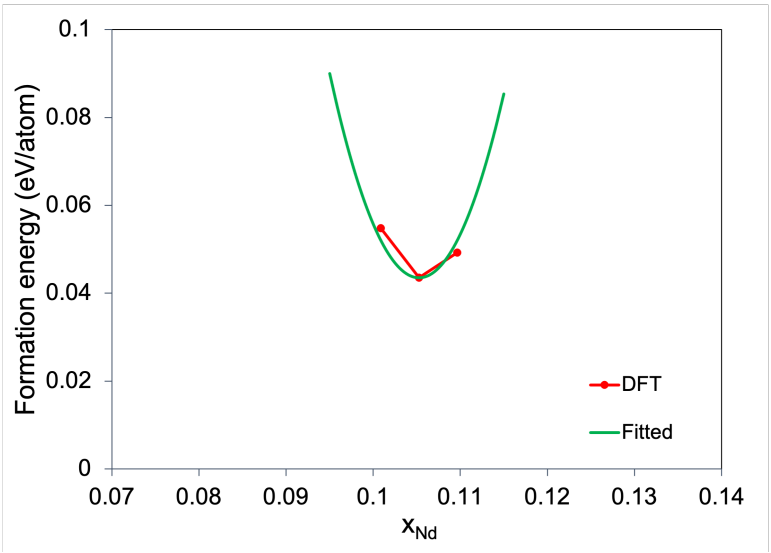

Figure 3.2. Fitting the formation energies of perfect and defective $Fe_{17}Nd_2$ using a parabola.

3.2 Modeling of Nd Diffusion in Bulk Bcc Fe

3.2.1 DFT calculations

To obtain the bulk diffusivity of Nd in α-Fe mediated by the vacancy mechanism, we have performed DFT calculations using projector augmented wave (PAW) pseudopotentials and the generalized gradient approximation of Perdew-Burke-Ernzerhof (PBE) [9], as implemented in the Vienna ab initio simulation package (VASP) [10]. We have employed both 128-atom and 250-atom supercells to model α-Fe with various types of defects, which can be constructed via a 4×4×4 and 5×5×5 extension of the conventional bcc cubic unit cell, respectively. A large plane-wave cutoff energy of 400 eV and a 3×3×3 Monkhorst-Pack k-point mesh for Brillouin zone sampling are used to ensure high numerical accuracy. All structures are fully relaxed with respect to cell-internal atomic positions with the cell volume and shape held fixed, until the Hellmann-Feynman forces are less than 0.02 eV/Å. By assuming ferromagnetic ordering of the magnetic moments of all Fe atoms in our spin-polarized calculations, the effects of ferromagnetic–paramagnetic transition of bcc Fe near its Curie temperature ($T_C = 1043$ K) has not been considered in this work.

For validation purposes, we first calculate the formation energy and formation entropy of a monovacancy in bcc Fe using the following equations:

$$E_f^V = E\left(Fe_{N-1}V_1\right) - \frac{N-1}{N}E\left(Fe_N\right) \tag{3.1}$$

$$S_f^V = S\left(Fe_{N-1}V_1\right) - \frac{N-1}{N}S\left(Fe_N\right) \tag{3.2}$$

where N is the number of lattice sites in the perfect supercell. $E\left(Fe_{N-1}V_1\right)$ and $S\left(Fe_{N-1}V_1\right)$ are the total energy and entropy of bcc Fe supercells containing a monovacancy, respectively. $E\left(Fe_N\right)$ and $S\left(Fe_N\right)$ are, respectively, the total energy and entropy of a perfect bcc Fe supercell. The entropy of a structure due to lattice vibrations is obtained using the force-constant approach within the harmonic approximation, as implemented in phonopy code [11]. The interatomic force constant matrices are fitted to quantum mechanical forces in large perturbed supercells with the magnitude of atom displacements set at 0.02 Å. For each wave vector in the Brillouin zone, one can construct a dynamical matrix using the fitted force constants, and the solution of the eigenvalue problem gives the phonon frequencies. An integration over the Brillouin zone gives the phonon density of states, from which the harmonic vibrational entropy of a structure can be calculated. As shown in Table 3.1, our calculations of the vacancy formation energy in bcc Fe using 128-atom and 250-atom supercells yield very similar results, which also agree well with previous DFT studies [12, 13, 14]. While our phonon calculations using 250-atom supercells give vacancy formation entropy that is larger than the values reported by Lucas and Schaublin [12], Messina et al. [15], and Versteylen et al. [14], the vacancy formation entropy obtained by our 128-atom calculations is in closer agreement with the previous DFT studies.

We obtain the binding energy of a Nd+nV complex, which contains a Nd substitutional atom and n monovacancies, as follows:

$$E_b^{Nd+nV} = E\left(Fe_{N-n-1}Nd_1V_n\right) + nE\left(Fe_N\right) - E\left(Fe_{N-1}Nd_1\right) - nE\left(Fe_{N-1}V_1\right) \tag{3.3}$$

Table 3.1. DFT calculated formation energy and formation entropy of a monovacancy in α-Fe.

Supercell size	**Formation energy (eV)**	**Formation entropy (k_B)**
N=250	2.203 (this work)	5.25 (this work), 4.62 [15]
N=128	2.176 (this work), 2.16 [12], 2.18 [13]	4.62 (this work), 4.08 [12], 4.83 [15]
N=128	2.129 [14]	4.14 [14]

Table 3.2. DFT calculated binding energies and binding entropies of Nd-vacancy defect complexes in α-Fe.

Nd-vacancy complex	**Binding energy (eV)**	**Binding entropy (k_B)**
Nd+V	-1.768	-0.07
Nd+2V	-3.411	-0.72
Nd+3V	-5.592	-2.71
Nd+4V	-6.922	-4.25
Nd+5V	-8.495	-5.57

where $E\left(Fe_{N-n-1}Nd_1V_n\right)$ and $E\left(Fe_{N-1}Nd_1\right)$ are the total energies of bcc Fe supercells containing a Nd+nV and a Nd substitutional defect, respectively. By this definition, a negative binding energy indicates attraction between individual point defects, and a positive binding energy suggests that there is a thermodynamic driving force for spontaneous cluster dissociation.

The binding entropy of a Nd+nV complex can be similarly calculated as follows:

$$S_b^{Nd+nV} = S\left(Fe_{N-n-1}Nd_1V_n\right) + nS\left(Fe_N\right) - S\left(Fe_{N-1}Nd_1\right) - nS\left(Fe_{N-1}V_1\right) \tag{3.4}$$

Our DFT calculated binding energies and binding entropies of Nd+nV defects in their respective ground-state (GS) configurations are summarized in Table 3.2. Here, we search for the ground-state defect configurations using the "round up the usual suspects" approach, i.e. by enumerating symmetrically distinct ways of distributing a given number of monovacancies around one Nd substitutional. The GS structures of Nd+nV defects for n between 1 and 5 are shown in Figure 3.3. In the GS structures, a Nd atom occupies an off-lattice position either between a pair of vacancies or at the center of a vacancy cluster. Importantly, the very negative binding energies suggest strong binding between monovacancies and Nd substitutionals. Furthermore, the magnitude of the binding energy for a Nd+nV cluster increases continuously with n, which implies that a Nd substitutional can attract multiple monovacancies to form thermodynamically stable Nd-vacancy complexes.

3.2.2 Equilibrium concentrations of defect complexes in dilute bcc Fe-Nd alloy

Using the results from Table 3.2, we calculate the equilibrium defect concentrations in a dilute bcc Fe-Nd alloy by solving the following equations according to the mass action law:

$$c_{eq}^V = \exp\left(\frac{S_f^V}{k_B}\right)\exp\left(-\frac{E_f^V}{k_BT}\right) \tag{3.5}$$

$$c_{eq}^{Nd+V} = 4\exp\left(\frac{S_b^{Nd+V}}{k_B}\right)\exp\left(-\frac{E_b^{Nd+V}}{k_B T}\right)c_{eq}^{Nd}\,c_{eq}^{V} \tag{3.6}$$

$$c_{eq}^{Nd+2V} = 12\exp\left(\frac{S_b^{Nd+2V}}{k_B}\right)\exp\left(-\frac{E_b^{Nd+2V}}{k_B T}\right)c_{eq}^{Nd}\left(c_{eq}^{V}\right)^2 \tag{3.7}$$

$$c_{eq}^{Nd+3V} = 6\exp\left(\frac{S_b^{Nd+3V}}{k_B}\right)\exp\left(-\frac{E_b^{Nd+3V}}{k_B T}\right)c_{eq}^{Nd}\left(c_{eq}^{V}\right)^3 \tag{3.8}$$

$$c_{eq}^{Nd+4V} = 12\exp\left(\frac{S_b^{Nd+4V}}{k_B}\right)\exp\left(-\frac{E_b^{Nd+4V}}{k_B T}\right)c_{eq}^{Nd}\left(c_{eq}^{V}\right)^4 \tag{3.9}$$

$$c_{eq}^{Nd+5V} = 3\exp\left(\frac{S_b^{Nd+5V}}{k_B}\right)\exp\left(-\frac{E_b^{Nd+5V}}{k_B T}\right)c_{eq}^{Nd}\left(c_{eq}^{V}\right)^5 \tag{3.10}$$

$$c_{eq}^{Nd} + c_{eq}^{Nd+V} + c_{eq}^{Nd+2V} + c_{eq}^{Nd+3V} + c_{eq}^{Nd+4V} + c_{eq}^{Nd+5V} = c_{total}^{Nd} \tag{3.11}$$

where k_B is the Boltzmann constant. The first term on the right-hand sides of equations 3.6, 3.7, 3.8, 3.9, and 3.10 is the multiplicity (number of indistinguishable configurations per lattice site) of the respective defect complex. c_{eq}^{V} is the equilibrium concentration of isolated vacancies. c_{eq}^{Nd} is the equilibrium concentration of Nd substitutionals that are not bound to vacancies. c_{total}^{Nd} is the total concentration of Nd in the Fe-Nd alloy and will take a constant value of 0.01% in the present calculations.

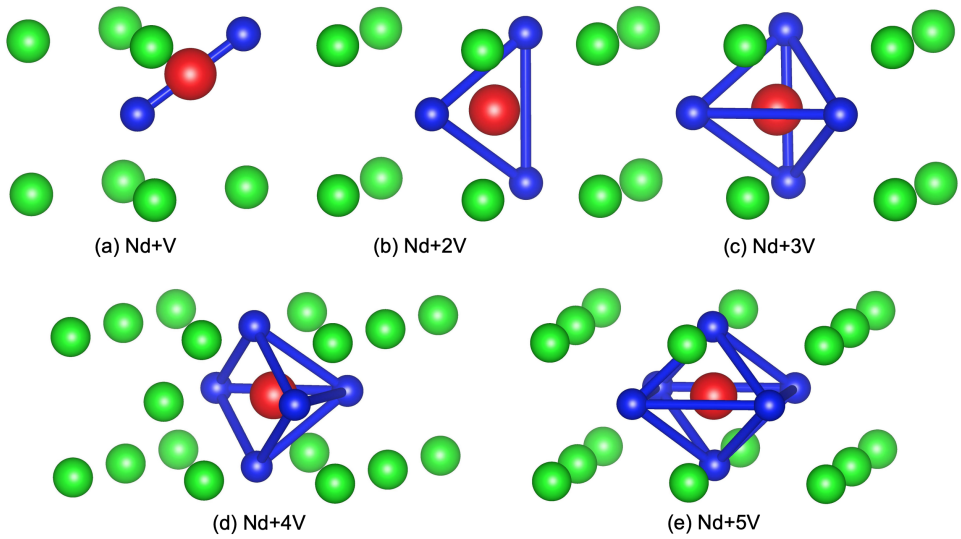

Figure 3.3. Ground-state configurations of Nd+nV defect complexes in α-Fe. Green and red spheres represent Fe and Nd atoms, respectively. Blue spheres represent a vacancy or a half-vacancy.

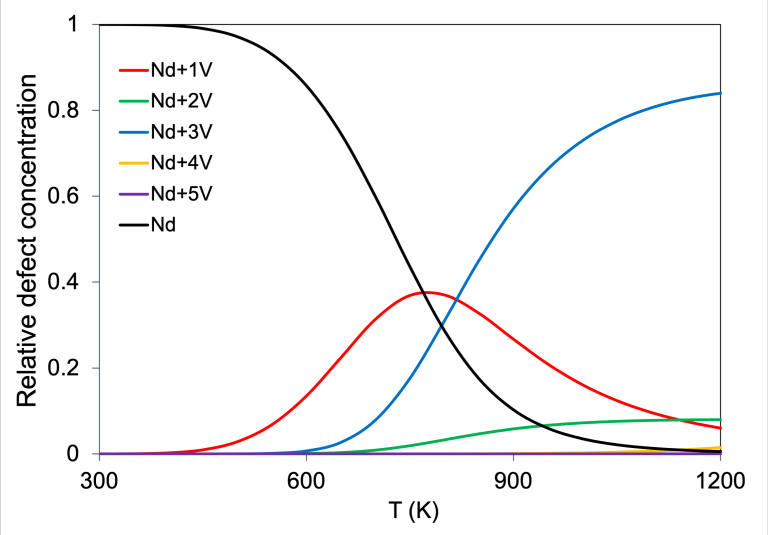

Figure 3.4. Relative concentrations of Nd+nV defects in dilute bcc Fe-Nd alloy.

Figure 3.4 shows the calculated relative concentrations of Nd+nV defect complexes in dilute bcc Fe-Nd alloy, defined as the defect concentration divided by the total Nd concentration, i.e. $c_{rel}^{Nd+nV} = c_{eq}^{Nd+nV} / c_{total}^{Nd}$. The advantage of using relative defect concentrations is that they can give a direct measure of the relative abundances of defect complexes as their values are independent of the total Nd concentration assumed in our calculations. While Nd and Nd+V dominate at low temperatures, Nd+3V, Nd+2V, and Nd+V are the most abundant defects at high temperatures. Interestingly, with increasing temperature, the relative concentration of Nd+V first increases due to the increase in monovacancy concentration, but then decreases with temperature after reaching its peak value at ~780 K, which is due to the emergence of larger Nd+nV clusters at the expense of Nd+V.

3.2.3 KMC simulations

According to transition state theory, the hopping rate of a defect can be calculated using the Arrhenius equation:

$$\Gamma = \nu_0 \exp\left(-\frac{\Delta E_{mig}}{k_B T}\right) \tag{3.12}$$

where ν_0 is the attempt frequency and ΔE_{mig} is the energy barrier. We have employed a climbing image nudged elastic band (CI-NEB) method [16] with three intermediate images to obtain the minimum energy paths (MEPs) and associated ΔE_{mig} for the migration of Nd+V, Nd+2V, and Nd+3V defect complexes in α-Fe. Due to their low concentrations even at high temperatures (see Figure 3.4), the migration of Nd+4V and Nd+5V defects has not been considered in the present study. For the Nd+V defect, we have considered the diffusion mechanism in which a vacancy moves from a first-nearest-neighbor (1NN) position to a third-nearest-neighbor (3NN) position of a Nd substitutional atom (see Figure 3.5), followed by a reverse 3NN → 1NN jump. The same mechanism has been previously proposed by Mock and Abe [17] and by Bocquet et al. [18] for the diffusion of Y in bcc Fe. For the migration of the Nd+2V defect, we

Table 3.3. DFT calculated attempt frequencies and migration barriers for Nd-vacancy defect complexes in α-Fe.

Nd-vacancy complex	Path	Attempt frequency (THz)	Migration barrier (eV)
Nd+V	1NN → 3NN	3.62	1.778
Nd+V	3NN → 1NN	4.86	0.139
Nd+2V	Direct GS → GS	5.64	2.286
Nd+3V	GS → metastable	4.76	2.231
Nd+3V	Metastable → GS	4.57	0.927

have considered the path in which its GS structure is maintained after the jump (see Figure 3.6). Finally, in order for the Nd+3V defect to migrate, it will need to transform into a metastable configuration with a higher energy (see Figure 3.7). Repeated interconversions between the two configurations can lead to the long-range migration of the Nd+3V defect. The attempt frequency can be further calculated from the real vibrational frequencies of the initial state and the transition state. For computational efficiency, we have considered only the vibrational modes of the migrating atoms, with all other atoms held fixed [19]. Our final calculated attempt frequencies and migration barriers are summarized in Table 3.3.

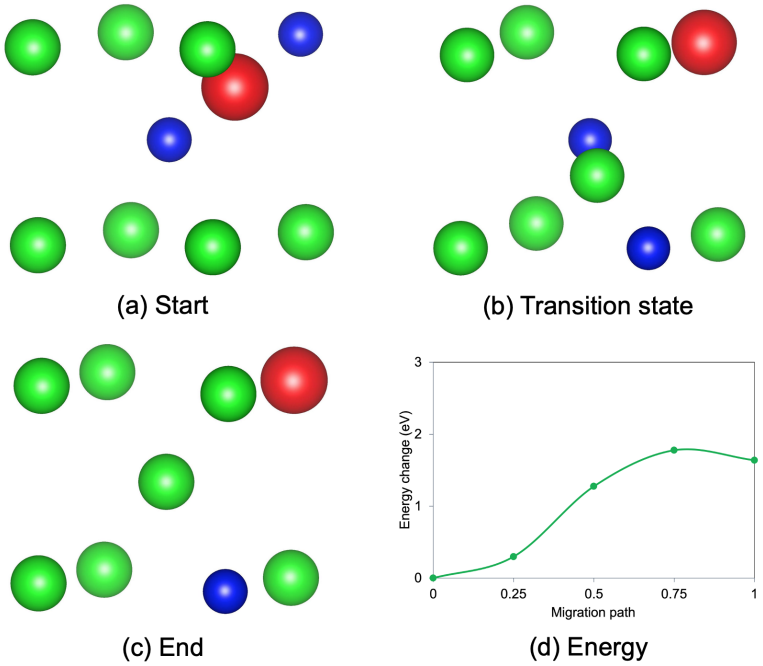

Figure 3.5. NEB calculated minimum energy diffusion path for Nd+V in α-Fe. In the start and end states, the vacancy is in a 1NN and 3NN position to a Nd substitutional atom, respectively. Green and red spheres represent Fe and Nd atoms, respectively. Blue spheres represent a vacancy or a half-vacancy. The energy changes along path are shown in (d).

Using the DFT calculated hopping rates as inputs, we have performed KMC simulations implementing a rejection-

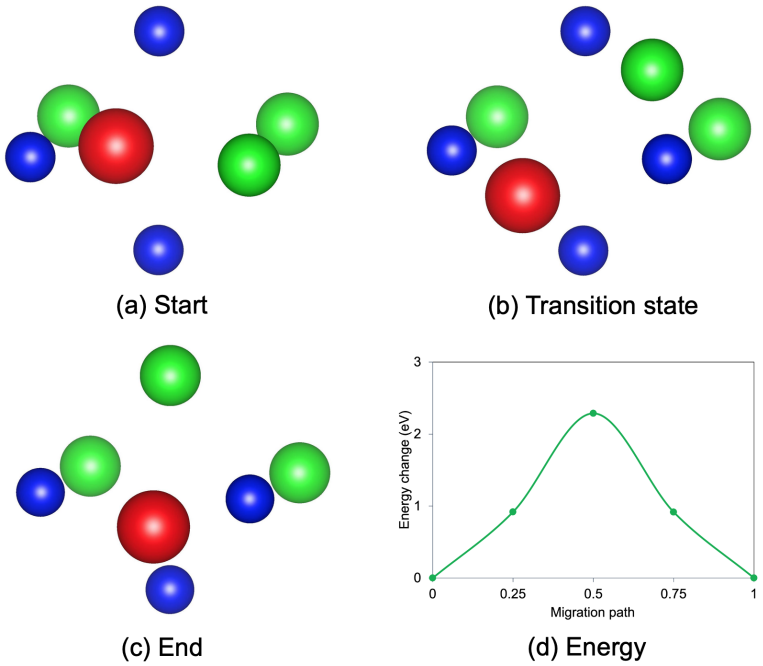

Figure 3.6. NEB calculated minimum energy diffusion path for Nd+2V in α-Fe. Both the start and end states correspond to the ground-state configuration of the defect complex, in which the Nd atom sits at the center of a trivacancy cluster. Green and red spheres represent Fe and Nd atoms, respectively. Blue spheres represent a vacancy or a half-vacancy. The energy changes along path are shown in (d).

free residence time algorithm [4] to compute the diffusivities of Nd+V, Nd+2V, and Nd+3V defect complexes in α-Fe. For each defect type, a total of 1000 non-interacting defects are used in our KMC simulations to generate mean squared displacement (MSD) data with good statistical accuracy, based on which diffusivity can be determined using the Einstein relation. At each KMC step, a random number is generated to pick one jump from a list of all possible jump events, with the average residence time given by the reciprocal of the sum of all rates. After the chosen jump is performed, the new position of the Nd atom within the Nd+nV defect is calculated. As shown in Figure 3.8, the diffusivities of Nd+V, Nd+2V, and Nd+3V defects all follow the Arrhenius relationship over a wide temperature range.

Finally, the total Nd diffusivity in α-Fe can be calculated as follows:

$$D_{total}^{Nd} = \sum_{n=1}^{3} c_{rel}^{Nd+nV} D_i^{Nd+nV} \tag{3.13}$$

where D_i^{Nd+nV} is the individual diffusivity of Nd+nV defect obtained from our KMC simulations. Our final results are shown in Figure 3.9. It can be seen that the total Nd diffusivity in α-Fe exhibits strongly non-Arrhenius behaviour. Two different temperature ranges can be identified in which $ln(D_{total}^{Nd})$ vs $1/T$ plot shows different slopes. At low temperatures, the diffusion of Nd is mainly mediated by Nd+V defects. While isolated Nd substitutional atoms are the dominant defect in this temperature regime, they are immobile and do not contribute to Nd diffusion. With increasing

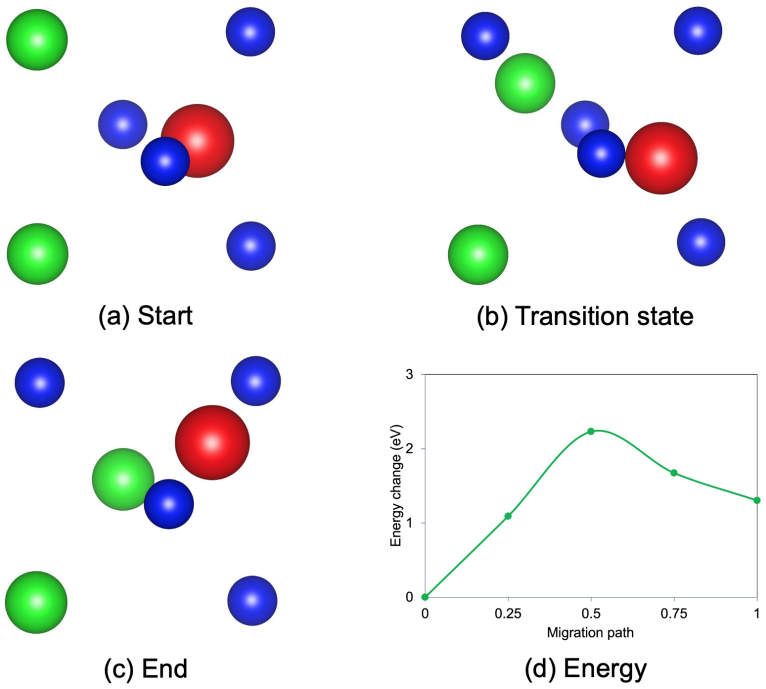

Figure 3.7. NEB calculated minimum energy diffusion path for Nd+3V in α-Fe. The start state corresponds to the ground-state configuration of the defect complex, in which the Nd atom sits at the center of a tetravacancy cluster. The end state corresponds to a metastable configuration. Green and red spheres represent Fe and Nd atoms, respectively. Blue spheres represent a vacancy or a half-vacancy. The energy changes along path are shown in (d).

temperature, the concentration of Nd+V continuously increases according to Equation 3.6. In this temperature regime, the Nd diffusivity can be approximately calculated as:

$$D_{total}^{Nd} \approx 4 \exp\left(\frac{S_b^{Nd+V} + S_f^V}{k_B}\right) \exp\left(-\frac{E_b^{Nd+V} + E_f^V}{k_B T}\right) D_i^{Nd+V} \tag{3.14}$$

As shown in Figure 3.9, this simple equation works very well for temperatures below ~650 K. At higher temperatures, equation 3.14 will be inapplicable since Nd+2V and Nd+3V will also be present in abundance under thermal equilibrium condition (see Figure 3.4). Since both Nd+2V and Nd+3V diffuse much slower than Nd+V (see Figure 3.8), the transition from Nd+V to these larger defect complexes will significantly slow down the diffusion of Nd atoms, which is the origin of the strong departure from the Arrhenius law observed in Figure 3.9.

For comparison, Figure 3.9 also shows the self-diffusivities of Fe, which can be calculated analytically as follows:

$$D_{self}^{Fe} = f \nu_0 a_{bcc}^2 \exp\left(\frac{S_f^V}{k_B}\right) \exp\left(-\frac{E_f^V + \Delta E_{mig}^V}{k_B T}\right) \tag{3.15}$$

where f=0.727 is the correlation factor for bcc structure, a_{bcc}=2.83 Å is the equilibrium lattice constant of α-Fe,

ν_0=4.6×10^{12} Hz is the attempt frequency for vacancy jump, and ΔE^V_{mig}=0.667 eV is the vacancy migration barrier from our DFT-NEB calculations. Except at high temperatures where the Nd mobility is strongly reduced due to the significant decline of Nd+V defect concentration, Nd diffusion in α-Fe is many orders of magnitude faster than Fe self-diffusion. The interdiffusion coefficient of dilute bcc Fe-Nd alloys can therefore be approximated by D^{Nd}_{total} with high precision.

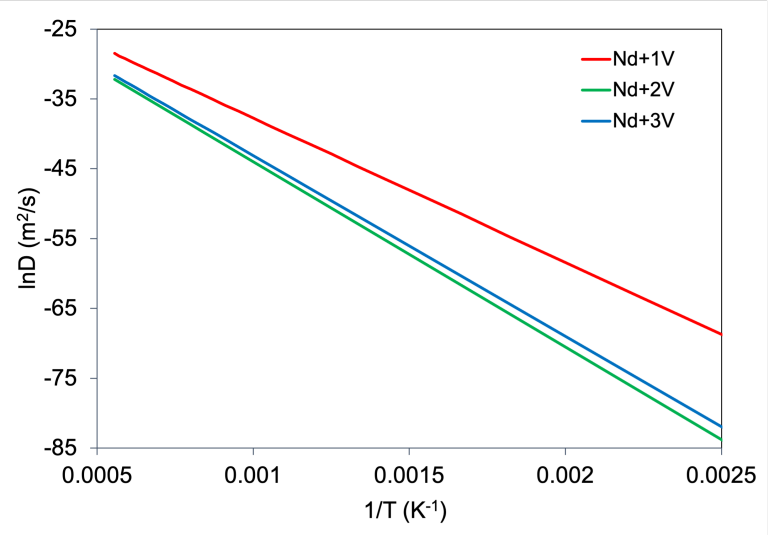

Figure 3.8. Arrhenius plot for the diffusivities of Nd+V, Nd+2V, and Nd+3V defects in α-Fe obtained from the present KMC simulations.

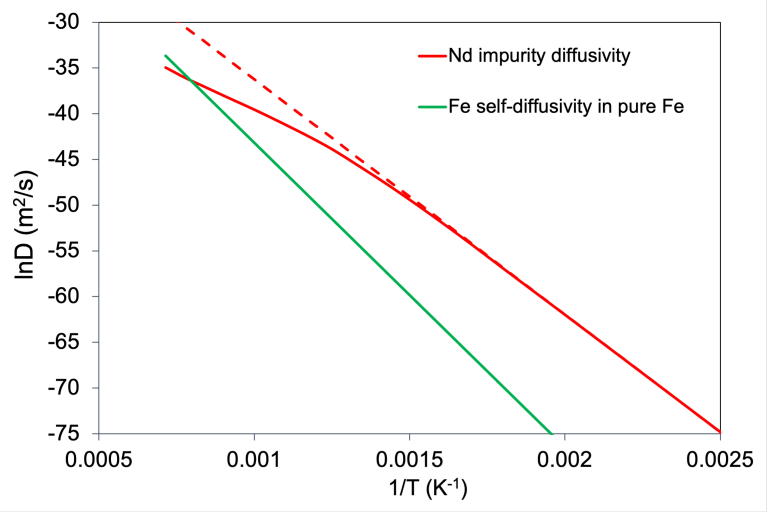

Figure 3.9. The total Nd diffusivity in α-Fe in comparison with the Fe self-diffusivity in α-Fe. The dashed line represents calculations using Equation 3.14.

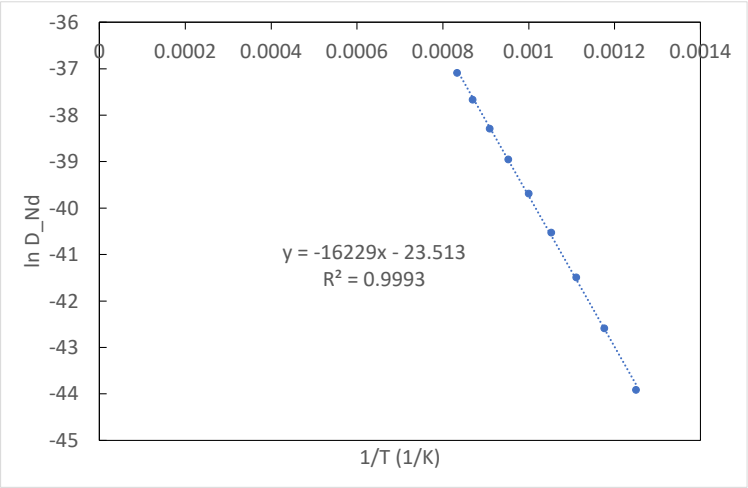

Figure 3.10. Arrhenius fit of the Nd diffusivities at higher temperatures.

Because the diffusivity of Nd deviates from Arrhenius behavior at higher temperatures, a separate function was fit to describe the high-temperature region of the Nd diffusivity in Figure 3.9. In this regime, from 800 K to 1200 K, an Arrhenius function with a different prefactor and activation energy was found to describe the diffusivity well. A plot of the data and corresponding function fit to the data is shown in Figure 3.10. In this regime, the diffusivity of Nd in the bulk of the matrix D^m_{Nd} is given by $D^m_{Nd} = D^m_{Nd,0} \exp\left(-E^m_a/kT\right)$, with $D^m_{Nd,0} = 6.14 \times 10^{-11}$ m^2/s and $E^m_a = 1.40$ eV.

4. PHASE-FIELD MODEL OF INTERMETALLIC PHASE FORMATION AND GROWTH

In this chapter, the phase-field model of the Fe-Nd system is described. The model is based on the grand potential formulation of Ref. [20]. In the current implementation, only two phases in the system are considered: the bcc Fe phase with Nd in solid solution and the $Fe_{17}Nd_2$ intermetallic phase. However, the model can be extended to additional phases in the system using the general formulation of Ref. [20], and also to additional chemical components. Using multiple order parameters, the current version of the model can simulate multiple grains of each of these phases. Each grain of the bcc Fe matrix phase is represented by an order parameter η_{mj}, where j indexes the individual grains of that phase. Within a grain, the corresponding order parameter $\eta_{mj} = 1$ and all other order parameters $\eta_{mk,k\neq j} = 0$. Similarly, each grain of the intermetallic phase is represented by an order parameter η_{il}. The number density of Nd atoms is given by ρ_{Nd}. The local normalized concentration (mole fraction) of Nd atoms is given by $c_{Nd} = \rho_{Nd}/V_a$, where V_a is the atomic volume of lattice sites. V_a is assumed to be the same between both phases in the phase-field model, and is given by the total unit cell volume of $Fe_{17}Nd_2$ of 0.797 nm^3 [21] divided by the 57 atoms in the unit cell, resulting in $V_a = 0.01398$ nm^3.

4.1 Phase-field Model Formulation and Parameterization

4.1.1 Grand potential functional

The evolution equations are derived from a functional of the grand potential densities that gives the total grand potential of the system, Ω:

$$\Omega = \int_V \left(\omega_{mw} + \omega_{grad} + \omega_{chem}\right) dV \tag{4.1}$$

where ω_{mw} is the multiwell grand potential density with respect to the order parameters, ω_{grad} is the gradient energy grand potential density, and ω_{chem} is the grand potential density due to chemical contribution. ω_{mw} is given by [22]

$$\omega_{mw} = m f_0 \tag{4.2}$$

$$f_0 = \sum_{\alpha=m,i} \sum_{j=1}^{p_\alpha} \left(\frac{\eta_{\alpha j}^4}{4} - \frac{\eta_{\alpha j}^2}{2}\right) + \sum_{\alpha=m,i} \sum_{j=1}^{p_\alpha} \left(\sum_{\beta=m,i} \sum_{j=1,\alpha j\neq\beta k}^{p_\beta} \frac{\gamma_{\alpha j\beta k}}{2} \eta_{\alpha j}^2 \eta_{\beta k}^2\right) + \frac{1}{4} \tag{4.3}$$

where α and β index phases, j and k index grains, p_α is the number of grains of phase α, and $\gamma_{\alpha j \beta k}$ is a set of constants that can be used to adjust the interfacial energy and thickness. ω_{grad} is given by

$$\omega_{grad} = \frac{\kappa}{2}\left(\sum_{j=1}^{p_m}\left|\nabla\eta_{mj}\right|^2 + \sum_{k=1}^{p_i}\left|\nabla\eta_{ik}\right|^2\right) \tag{4.4}$$

where κ is the gradient energy coefficient, with dimensions of energy per unit length. ω_{chem} is given by

$$\omega_{chem} = h_m\omega_m + h_i\omega_i \tag{4.5}$$

where h_m and h_i are interpolation functions and ω_m, ω_i are the grand potential densities for the bulk matrix and intermetallic phases. The interpolation functions are given by

$$h_m = \frac{\sum_{j=1}^{p_m}\eta_m^2}{\sum_{j=1}^{p_m}\eta_m^2 + \sum_{k=1}^{p_i}\eta_i^2} \tag{4.6}$$

$$h_i = \frac{\sum_{k=1}^{p_i}\eta_i^2}{\sum_{j=1}^{p_m}\eta_m^2 + \sum_{k=1}^{p_i}\eta_i^2} \tag{4.7}$$

The grand potential densities for each phase are given by

$$\omega_m = f_m - \rho_{Nd}\mu_{Nd} \tag{4.8}$$

$$\omega_b = f_b - \rho_{Nd}\mu_{Nd} \tag{4.9}$$

where f_m and f_i are the Helmholtz free energy densities of the matrix and intermetallic phases and μ_{Nd} is the chemical potential of Nd. Parabolic approximations are used for the dependence of f_m and f_i on c_{Nd}:

$$f_m = k_{Nd}^m(c_{Nd} - c_{Nd}^{m,min})^2 + f_0^m \tag{4.10}$$

$$f_i = k_{Nd}^i(c_{Nd} - c_{Nd}^{i,min})^2 + f_0^i \tag{4.11}$$

where k_{Nd}^m, k_{Nd}^i are the curvatures of the parabolas, $c_{Nd}^{m,min}$, $c_{Nd}^{i,min}$ are the minima of the parabolas, and f_0^m, f_0^i are constant offsets in the free energies.

4.1.2 Free Energy Parameterization

The parameterization of the bulk free energy of each phase is discussed first. In Section 3.1, the curvature of the parabolic approximation to the intermetallic phase free energy was found to be $k_{Nd}^i = 4.26 \times 10^7$ J/mol. The molar volume of $Fe_{17}Nd_2$, V_m, can by found from $V_m = V_a N_a$, where N_a is Avogadros's number, resulting in $V_m = 8.42{\times}10^{-6}$ m^3/mol. This can be used to put k_{Nd}^i into units of J/m^3, resulting in $k_{Nd}^i = 5.06 \times 10^{12}$ J/m^3. The minimum of the parabolic approximation $c_{Nd}^{i,min}$ is at Nd composition of $2/19 = 0.0105$. From CALPHAD data [7], the formation

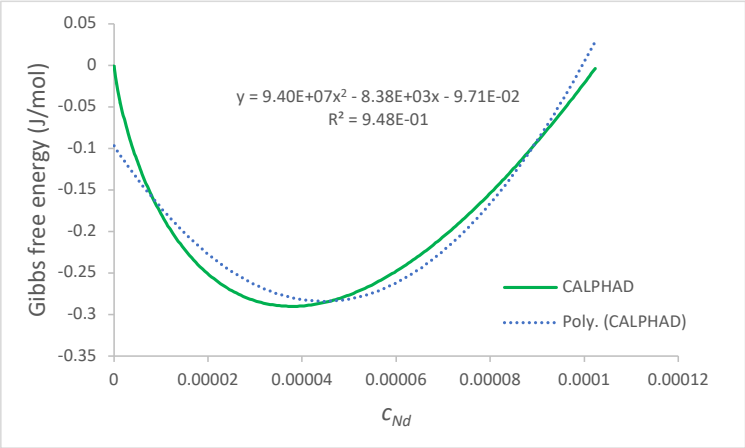

Figure 4.1. Free energy of bcc Fe phase as a function of c_{Nd} from CALPHAD data and corresponding second-order polynomial (parabolic) fit.

energy of the $Fe_{17}Nd_2$ phase is $f_0^i = -3.9 \times 10^8$ J/m^3 relative to the pure bcc Fe reference state.

To obtain an approximation for the bcc Fe matrix phase, a parabolic function was fit to the CALPHAD data for free energy versus c_{Nd}. The CALPHAD data and corresponding parabolic fit are shown in Figure 4.1. Although a third-order polynomial was found to fit the data better, the second-order parabolic function is required for use in the grand potential formulation, and fit the data reasonably well. The standard-form equation shown in Figure 4.1 was converted to vertex form, resulting in $k_{Nd}^m = 9.4 \times 10^7$ J/mol, $c_{Nd}^{m,min} = 4.45 \times 10^{-5}$, and $f_0^m = -0.284$ J/mol. Using the molar volume of bcc Fe as 8.42×10^{-6} m^3/mol to convert units results in $k_{Nd}^m = 1.34 \times 10^{13}$ J/m^3 and $f_0^m = -4.03 \times 10^4$ J/m^3.

The grain boundary energies, interfacial energies, and interface widths in this system are used to determine the model parameters κ and m. The mean grain boundary energy between grains in bcc Fe is estimated as $\sigma_{mm} = 1.11$ J/m^2 [23]. The grain boundaries in the model are represented by the diffuse interface between order parameters such as η_{mj} and η_{mk}. For such an interface, if the constant γ_{mjmk} from Equation 4.3 is chosen as $\gamma_{mjmk} = 1.5$, the following analytical relationships exist [20]:

$$\kappa = \frac{3}{4}\sigma_{mm} l_{int} \tag{4.12}$$

$$m = \frac{6\sigma_{mm}}{l_{int}} \tag{4.13}$$

where l_{int} is the characteristic thickness of the diffuse interface. Based on preliminary data from atom probe tomography, we set $l_{int} = 6$ nm, resulting in $\kappa = 5.00 \times 10^{-9}$ J/m and $m = 1.11 \times 10^9$ J/m^3.

To our knowledge, the interfacial energy between the matrix and intermetallic phases σ_{mi} and the grain boundary energy of the intermetallic σ_{ii} have not yet been determined; thus for simplicity we set $\sigma_{ii} = \sigma_{im} = \sigma_{mm} = 1.11$ J/m^2. With this choice, the value of all constants $\gamma_{\alpha j \beta k}$ can be set to 1.5; however, if data on σ_{ii} and σ_{im} become available in the future, the correct values can be set by setting the constants $\gamma_{\alpha j \beta k}$ using the process described in Ref. [20].

4.1.3 Evolution Equations

The order parameter for each grain of the matrix phase evolves by the Allen-Cahn equation, derived from the grand potential functional of Equation 4.1:

$$\frac{\partial \eta_{mj}}{\partial t} = -L \frac{\delta \Omega}{\delta \eta_{mj}} \tag{4.14}$$

where L is the mobility coefficient. A similar Allen-Cahn equation exists for each order parameter for the intermetallic phase:

$$\frac{\partial \eta_{ij}}{\partial t} = -L \frac{\delta \Omega}{\delta \eta_{ij}} \tag{4.15}$$

In the grand potential formulation, the evolution equation for Nd density is transformed into an evolution equation for μ_{Nd} [20]:

$$\frac{\partial \mu_{Nd}}{\partial t} = \frac{1}{\chi_{Nd}} \left[\nabla \cdot \left(M_{Nd} \nabla \mu_{Nd} \right) - \sum_{\alpha=m,i} \sum_{j=1}^{p_\alpha} \frac{\partial \rho_{Nd}}{\partial \eta_{\alpha j}} \frac{\partial \eta_{\alpha j}}{\partial t} \right] \tag{4.16}$$

where χ_{Nd} is the susceptibility and M_{Nd} is the mobility of Nd atoms. The susceptibility $\chi_{Nd} \equiv \frac{\partial \rho_{Nd}}{\partial \mu_{Nd}}$, and for the parabolic free energy form used here is given by [20]:

$$\chi_{Nd} = h_m \chi^m_{Nd} + h_i \chi^i_{Nd} \tag{4.17}$$

with the susceptibilities of each phase given by

$$\chi^m_{Nd} = \frac{1}{V_a^2 k^m_{Nd}} \tag{4.18}$$

and

$$\chi^i_{Nd} = \frac{1}{V_a^2 k^i_{Nd}} \tag{4.19}$$

The mobility M_{Nd} can be different in each phase, and is given by

$$M_{Nd} = h_m M^m_{Nd} + h_i M^i_{Nd} \tag{4.20}$$

where $M^m_{Nd} = D^m_{Nd} \chi^m_{Nd}$ and $M^i_{Nd} = D^i_{Nd} \chi^i_{Nd}$, with D^m_{Nd} and D^i_{Nd} the diffusivities of Nd atoms in the matrix and intermetallic phases, respectively. The density of Nd atoms in the last term of Equation 4.16 is given by interpolation of the density of Nd atoms in each phase:

$$\rho_{Nd} = h_m \rho^m_{Nd} + h_i \rho^i_{Nd} \tag{4.21}$$

The density of Nd atoms ρ_{Nd} in each phase is a function of the local chemical potential and the parameters of the parabolic free energy [20]:

$$\rho^m_{Nd} = \frac{\mu_{Nd}}{V_a^2 k^m_{Nd}} + \frac{c^{m,min}_{Nd}}{V_a} \tag{4.22}$$

$$\rho^i_{Nd} = \frac{\mu_{Nd}}{V_a^2 k^i_{Nd}} + \frac{c^{i,min}_{Nd}}{V_a} \tag{4.23}$$

The parameterization of parabola curvatures k^m_{Nd}, k^i_{Nd} and minima $c^{m,min}_{Nd}$, $c^{i,min}_{Nd}$ were discussed in Section 4.1.2. The diffusivity of Nd in the matrix phase D^m_{Nd} was taken from the atomistic calculations of Chapter 3, which showed that in the higher-temperature regime expected to be relevant for FCCI, $D^m_{Nd} = D^m_{Nd,0} \exp\left(-E^m_a/kT\right)$, with $D^m_{Nd,0} = 6.14 \times 10^{-11}$ m^2/s and $E^m_a = 1.40$ eV. The diffusivity of Nd atoms in the intermetallic $Fe_{17}Nd_2$ phase, D^i_{Nd}, was taken from experimental measurements of a Fe-Nd diffusion couple [24], which gave the diffusivity as $D^i_{Nd} = D^i_{Nd,0} \exp\left(-E^i_a/kT\right)$, with $D^i_{Nd,0} = 8 \times 10^{-7}$ m^2/s and $E^i_a = 1.32$ eV. For the diffusion couple simulations of Section 4.2.2, which were conducted at a temperature of 953 K or 680 °C, this results in $D^i_{Nd} = 8.4 \times 10^{-14}$ m^2/s and $D^m_{Nd} = 2.4 \times 10^{-18}$ m^2/s. It should be noted that it is unexpected that the $D^i_{Nd} >> D^m_{Nd}$. Given that the much more complex crystal structure of the intermetallic phase would likely make atomic jumps of Nd atoms from one vacant Nd site to another more difficult, it would be expected that the diffusivity of Nd in the intermetallic phase would be lower than that in the bcc Fe matrix. It is possible that Nd atoms diffuse on vacant Fe sites in $Fe_{17}Nd_2$ rather than, or in addition to, diffusing on vacant Nd sites. Future computational work may be used to shed light on the reason for unexpectedly high Nd diffusivity in the intermetallic $Fe_{17}Nd_2$ phase.

The evolution equations were non-dimensionalized using energy scale $E^* = 10^{11}$ J/m^3, length scale $l^* = 1$ nm. Different time scales τ^* were used in the following sections to maintain a non-dimensionalized Nd diffusivity $\bar{D}_{Nd}$ (the overbar indicates a non-dimensional quantity) of order one in at least one of the phases to optimize numerical performance. Finally, the mobility coefficient L in the Allen-Cahn equations 4.14 and 4.15 is set by making $\bar{L} = 10$ so that it is an order of magnitude greater that $\bar{D}_{Nd}$. This ensures that growth of the intermetallic phase is limited by the diffusion of Nd rather than by the mobility of the matrix-intermetallic interface. The dimensional value L can be determined based on the time scale using $L = \frac{\bar{L}}{E^* \tau^*}$. The parameters used in phase-field simulations are summarized in Table 4.1.

4.1.4 Numerical implementation

The evolution equations were discretized using the MOOSE framework. The spatial domain was discretized using 1D or 2D meshes with linear Lagrange shape functions. A mesh resolution of $\Delta x = \Delta y = 2$ nm was used to allow three elements through the interface based on the choice of $l_{int} = 6$ nm. The second-order accurate backward differentiation formula was used for time integration, with adaptive time stepping as implemented in the MOOSE IterationAdaptiveDT time stepper [25]. In this scheme, the time step is adapted to maintain the number of PETSc nonlinear solver iterations required to converge the solution to be within a user-specified range. In our case, a relative convergence tolerance of 10^{-8} was used, with an absolute tolerance of 10^{-10} for problems that approach a steady state, and the number of nonlinear iterations was maintained in the range 8 ± 2.

Parameter	Value
$c_{Nd}^{m,min}$	4.45×10^{-5}
$c_{Nd}^{i,min}$	0.0105
k_{Nd}^{m}	1.34×10^{13} J/m^3
k_{Nd}^{i}	5.06×10^{12} J/m^3
f_0^m	-4.03×10^{4} J/m^3
f_0^i	-3.9×10^{8} J/m^3
κ	5.00×10^{-9} J/m
m	1.11×10^{9} J/m^3
γ_{mjik}	1.5
γ_{mjmk}	1.5
γ_{ijik}	1.5
V_a	0.01398 nm^3
$D_{Nd,0}^{m}$	6.14×10^{-11} m^2/s
E_a^m	1.40 eV
$D_{Nd,0}^{i}$	8×10^{-7} m^2/s
E_a^i	1.32 eV
$\bar{L}$	10

Table 4.1. Phase-field model parameters.

4.2 Simulation Results

4.2.1 1D equilibrium simulations

Prior to performing simulations of the kinetics of the Fe-Nd system, the equilibrium behavior of the model is first verified using a 1D simulation along the x-direction of the interface between a grain of the matrix phase, represented by order parameter η_{m0}, and a grain of the intermetallic phase, represented by order parameter η_{i0}. In equilibrium, for $\gamma_{mjik} = 1.5$, the order parameter profiles are given by [20]

$$\eta_{i0} = \frac{1}{2}\left[1 - \tanh\left(\sqrt{\frac{m}{2\kappa}}\right)(x - x_0)\right] \tag{4.24}$$

$$\eta_{m0} = \frac{1}{2}\left[1 + \tanh\left(\sqrt{\frac{m}{2\kappa}}\right)(x - x_0)\right] \tag{4.25}$$

where x_0 is the midpoint of the interface in the x-direction. The other condition for equilibrium is that μ_{Nd} is constant throughout both phases. The common tangent construction between the two phases determines the equilibrium chemical potential. To estimate the chemical potential at equilibrium, the slope of the line connecting the minima of the free energies of the matrix and intermetallic phases on a plot of non-dimensionalized free energy versus composition, $\Delta\bar{f}/\Delta c_{Nd}$, was determined. This does not truly give the common tangent if the parabolic curvatures of the free energies of the two phases are different, but gives a good approximation if the curvatures are large. The determination

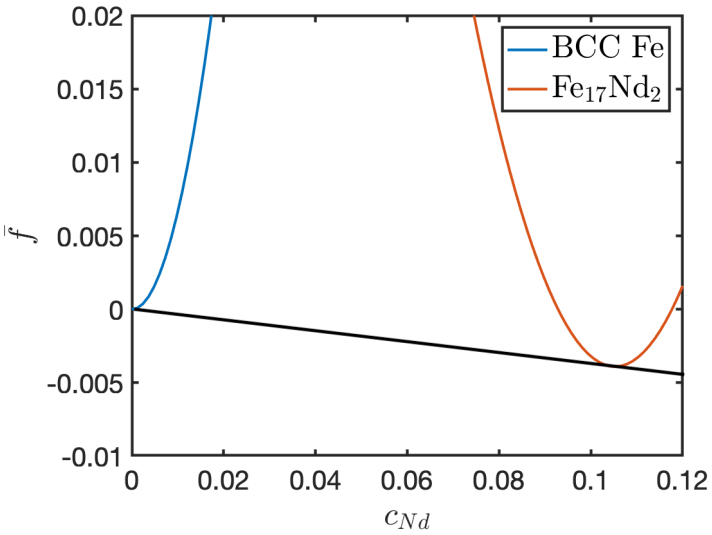

Figure 4.2. Non-dimensionalized free energies of the bcc Fe and $Fe_{17}Nd_2$ phases as a function of c_{Nd}. The equilibrium chemical potential of Nd for two-phase coexistence is estimated by determining the slope of line connecting the minima of the parabolic approximations, $\Delta\bar{f}/\Delta c_{Nd}$, as shown with the black line.

of $\Delta\bar{f}/\Delta c_{Nd}$ is shown schematically in Figure 4.2. Using this approximation, the equilibrium chemical potential can be estimated as [26]:

$$\bar{\mu_{Nd}} = \bar{V_a}\frac{\Delta\bar{f}}{\Delta c_{Nd}} = -5.18 \times 10^{-4} \tag{4.26}$$

Based on this, the initial conditions for the order parameters were set according to Equations 4.24 and 4.25, and the initial condition for the chemical potential was set to be a constant value of $\bar{\mu_{Nd}} = -5.18 \times 10^{-4}$ throughout the domain. The simulation domain ranged from $x = 0$ to $x = 80$, and thus $x_0 = 40$ in Equations 4.24 and 4.25. A time scale of $\tau^* = 1$ s was used. Since the steady-state conditions do not depend on the diffusion coefficients, to improve numerical performance, the same diffusion coefficient $D_{Nd} = 1.42 \times 10^{-18}$ m^2/s was used in both phases, based on the value in bcc Fe at 650°C. A short amount of time evolution was required to reach equilibrium since the initial chemical potential was based on an approximation to the common tangent construction. After that, the order parameter parameter profiles matched the equilibrium solutions well, as shown in Figure 4.3. When the simulation reached equilibrium, $\bar{\mu_{Nd}} = -5.19 \times 10^{-4}$. The resulting composition profile can be calculated from Equation 4.21 and the relation $c_{Nd} = \rho_{Nd} V_a$ and is shown in Figure 4.4.

4.2.2 Diffusion couple simulations and validation

With the equilibrium behavior of the model verified, in this section the model is used to simulate the 1D growth of a $Fe_{17}Nd_2$ layer in a diffusion couple at the interface between pure Nd (which also has the bcc crystal structure) and bcc Fe. The growth rate of the $Fe_{17}Nd_2$ layer is compared to the growth rate measured from experiment for validation

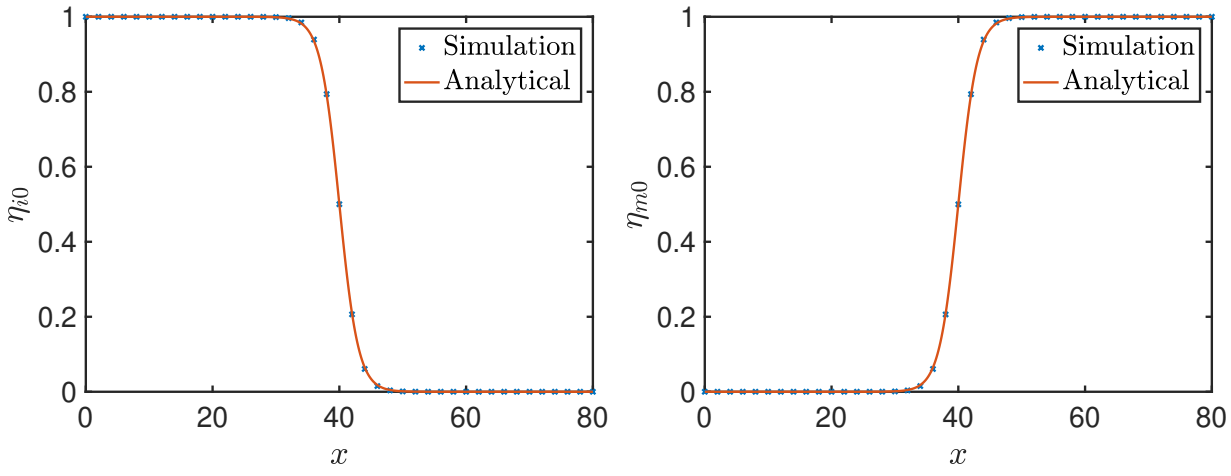

Figure 4.3. (a), (b). Comparison between simulation results and analytical solution of equilibrium order parameter profiles for matrix-intermetallic interface.

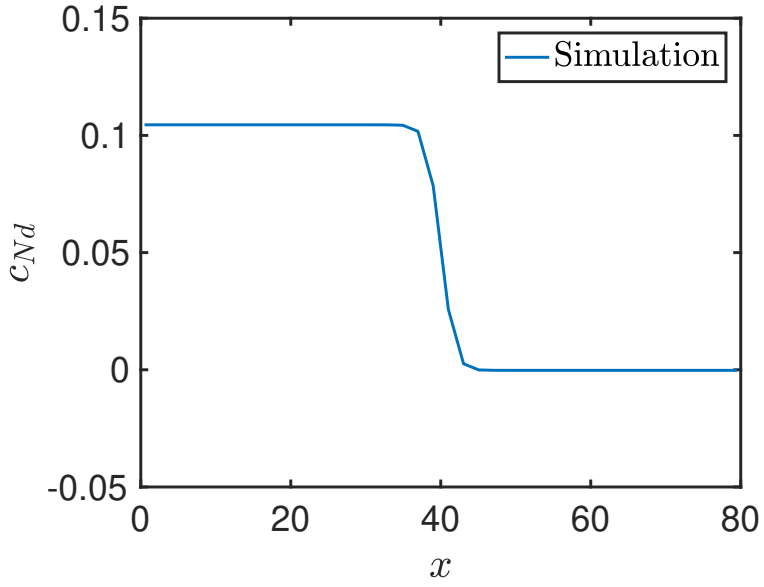

Figure 4.4. Equilibrium composition profile for Nd for a 1D interface between the intermetallic and matrix phase.

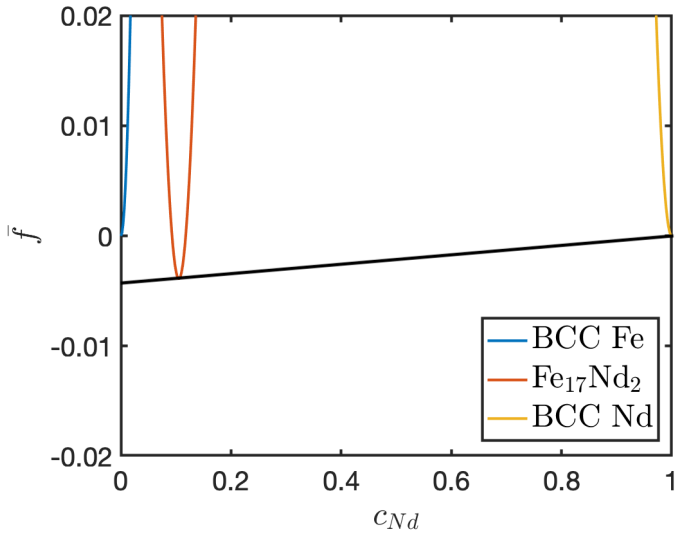

Figure 4.5. Non-dimensionalized free energies of the bcc Fe, $Fe_{17}Nd_2$, and bcc Nd phases as a function of c_{Nd}. For the diffusion couple simulations, the chemical potential at the left-side boundary (where the $Fe_{17}Nd_2$ is in contact with bcc Fe) is approximated by determining the slope of line connecting the minima of the free energies of these phases.

[24]. In the experiments, the growth rate of the $Fe_{17}Nd_2$ layer was parabolic, meaning that the thickness T follows an equation $T = Ct^{1/2}$, where C is a constant that depends on temperature and t is time.

This simulation was also conducted in 1D, with a domain ranging from $x = 0$ to $x = 500$ nm. A small layer of the $Fe_{17}Nd_2$ phase (6 nm thick) is assumed to exist in the initial conditions at the left-hand side of the simulation domain. Rather than expanding the model to consider the pure Nd phase explicitly, we instead set a boundary condition on μ_{Nd} at $x = 0$, assuming equilibrium between the $Fe_{17}Nd_2$ phase and bcc Nd. Given that the approximation for μ_{Nd} derived from the free energy plot in Figure 4.2 was within 0.25% of the equilibrium value, a similar approach was used to approximate μ_{Nd} at the bcc Nd-$Fe_{17}Nd_2$ interface. A schematic of the free energies of the different phases and the approximate chemical potential at the interface between bcc Nd and $Fe_{17}Nd_2$ are shown in Figure 4.5. Using this approach, the boundary condition $\bar{\mu_{Nd}} = 6.09\times10^{-5}$ was set at $x = 0$. Natural boundary conditions were used for μ_{Nd} on all other boundaries, such that the gradient of μ_{Nd} was zero and therefore no flux in or out of the system occurred at any other boundaries. Natural boundary conditions were also used for the order parameters. The initial conditions for the order parameters η_{m0} and η_{i0} were set using Equations 4.24 and 4.25, with $x_0 = 6$, and the initial condition for $\bar{\mu_{Nd}} = -5.18\times10^{-4}$ throughout.

Because the growth rate of the $Fe_{17}Nd_2$ phase is solely dependent on diffusion through $Fe_{17}Nd_2$, we use a uniform diffusion coefficient $D_{Nd} = 8\times10^{-14}$ m^2/s in both phases to improve computational efficiency, based on the diffusivity of Nd through $Fe_{17}Nd_2$ at 953 K, one of the temperatures at which diffusion couple data is available [24]. A time scale of $\tau^* = 10^{-5}$ s was used.

The thickness T of the $Fe_{17}Nd_2$ layer was determined from the simulations by calculating the distance from the left side of the simulation domain to the position at which $\eta_{i0} = 0.5$, the midpoint of the interface between the $Fe_{17}Nd_2$ and

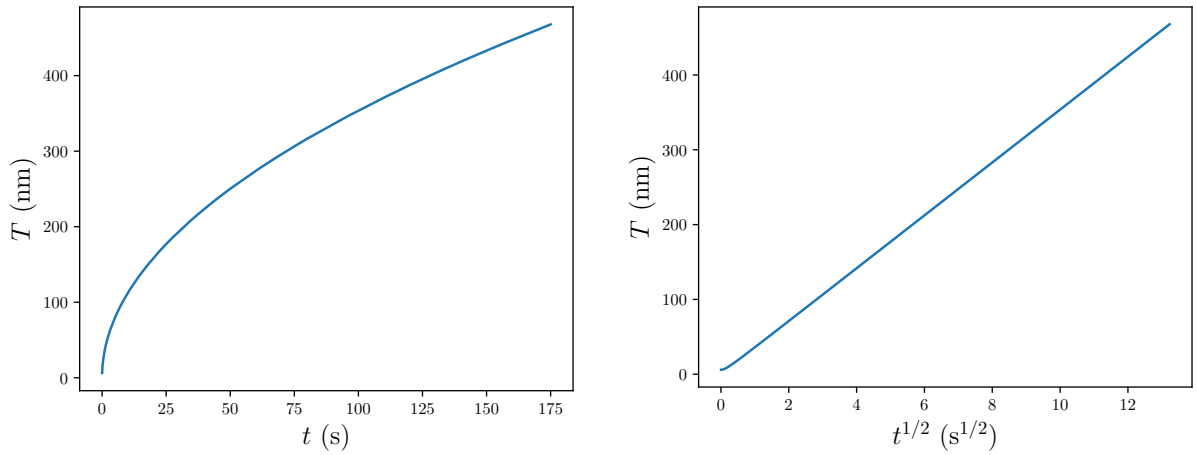

(a) (b)

Figure 4.6. Growth of $Fe_{17}Nd_2$ in a diffusion couple between bcc Fe and bcc Nd. Thickness T of the $Fe_{17}Nd_2$ layer is plotted versus (a) t and (b) $t^{1/2}$. The linear trend observed in (b) indicates that a parabolic growth law is followed.

bcc Fe phase. Thickness is plotted versus time in Figure 4.6a. If the thickness of the intermetallic follows the expected parabolic growth law $T = Ct^{1/2}$, then a plot of T versus $t^{1/2}$ should be linear. Figure 4.6b shows that after a short period of equilibration, the expected linear dependence is observed.

To compare the model to experiment, the slope of the line in Figure 4.6b was calculated for $t^{1/2} > 0.5$ $s^{1/2}$, resulting $C_{sim} = 3.53 \times 10^{-8}$ m/$s^{1/2}$. This can be compared to the experimentally measured value $C_{exp} = 5.83 \times 10^{-8}$ m/$s^{1/2}$ [24]. The simulation prediction is within 40% of the experimentally measured value, demonstrating reasonable agreement. The discrepancy may result partly from the fact that we have not modeled the diffusion of Fe back into the pure Nd phase as would occur in a real diffusion couple. It should also be noted that approximately 50% uncertainty was reported in the measured value of C [24], meaning that C could lie in the range $3.7 \times 10^{-8} < C < 6.6 \times 10^{-8}$.

4.2.3 Growth with grain boundary diffusion

In this section, the effect of grain boundaries on growth of the intermetallic phase is simulated. As discuseed in the Introduction, enhanced lanthanide diffusivity along grain boundaries is believed to result in the observed grain boundary attack by lanthanides in HT9 cladding that occurs further into the cladding than the fully formed FCCI layer. The diffusivities in the model are modified to account for this enhanced diffusivity. The diffusivity of Nd along grain boundaries in Fe has not been determined to our knowledge, but grain boundary (GB) diffusivity is typically 10^6 times greater than bulk diffusivity [27]. We include enhanced GB diffusivity in the model by making it a function of order parameters. For a two-grain configuration,

$$D^m_{Nd} = D^b_{Nd} + 16\eta^2_{m0}\eta^2_{m1}D^{GB}_{Nd} \tag{4.27}$$

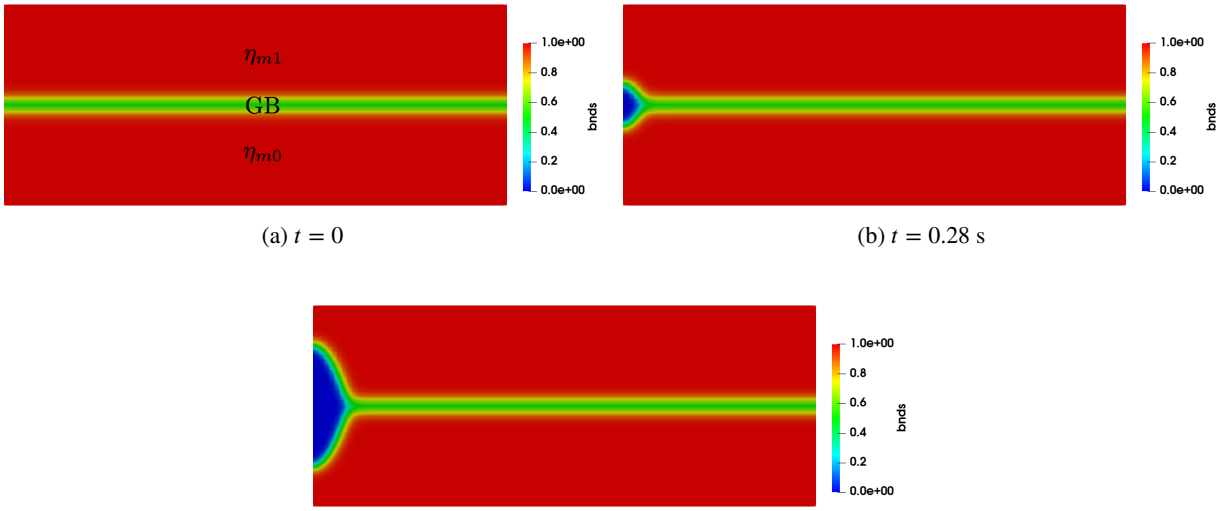

(a) $t = 0$ (b) $t = 0.28$ s

(c) $t = 0.38$ s

Figure 4.7. Simulations of Nd diffusion into a bicrystal, showing the evolution of microstructure. The initial conditions are shown in (a), and Nd diffuses in to the system from the boundary at the left hand side of the domain due to a Dirichlet boundary condition that maintains $\bar{\mu_{Nd}} = 6.09 \times 10^{-5}$. (b) The $Fe_{17}Nd_2$ phase forms spontaneously on the grain boundary at the left side of the domain. (c) Continued growth of the $Fe_{17}Nd_2$ phase occurs preferentially along the left side of the domain.

where the bulk diffusivity $D^b_{Nd} = 1.42 \times 10^{-18}$ m^2/s and the diffusivity of Nd in the intermetallic $Fe_{17}Nd_2$ phase is $D^i_{Nd} = 8 \times 10^{-14}$ m^2/s as before. The grain boundary diffusivity is assumed to be $D^{GB}_{Nd} = 8 \times 10^{-13}$ m^2/s, to ensure it was an order of magnitude greater than D^i_{Nd} so that GB diffusivity would be the dominant means of Nd transport in the simulation.

The initial microstructure of the simulation is shown in Figure 4.7a, which is a bicrystal domain of size 200 nm × 80 nm, with matrix grain 0 on the bottom and matrix grain 1 on the top and a grain boundary between them at $y = 40$ nm. There is no intermetallic phase present in the initial conditions. As in the diffusion couple simulations of Section 4.2.2, the initial chemical potential was set to $\bar{\mu_{Nd}} = -5.18 \times 10^{-4}$, and a boundary condition of $\bar{\mu_{Nd}} = 6.09 \times 10^{-5}$ was set at $x = 0$.

The evolution of c_{Nd} in the earlier stages of microstructural evolution is shown in Figure 4.8a – 4.8c. The enhanced diffusivity of Nd along the GBs leads to faster buildup of Nd along the GBs, as expected. At approximately $t = 0.25$ s, the $Fe_{17}Nd_2$ phase forms spontaneously where the grain boundary meets the left side of the simulation domain, where the concentration of Nd is highest. The microstructure just following this formation is shown in Figure 4.7b. With further evolution, the $Fe_{17}Nd_2$ phase grows from the initial nucleus outward, with more growth occurring along the left-hand domain boundary than along the grain boundary. This is inconsistent with the hypothesis that $Fe_{17}Nd_2$ forms a thin layer along the grain boundary. However, this may be because the boundary condition used here is based on a diffusion couple simulation, and therefore may be forcing much more Nd into the system along the boundaries than would occur in a FCCI situation. It could also indicate that the $Fe_{17}Nd_2$ exists as a grain boundary phase, which would necessitate changes to the model formulation.

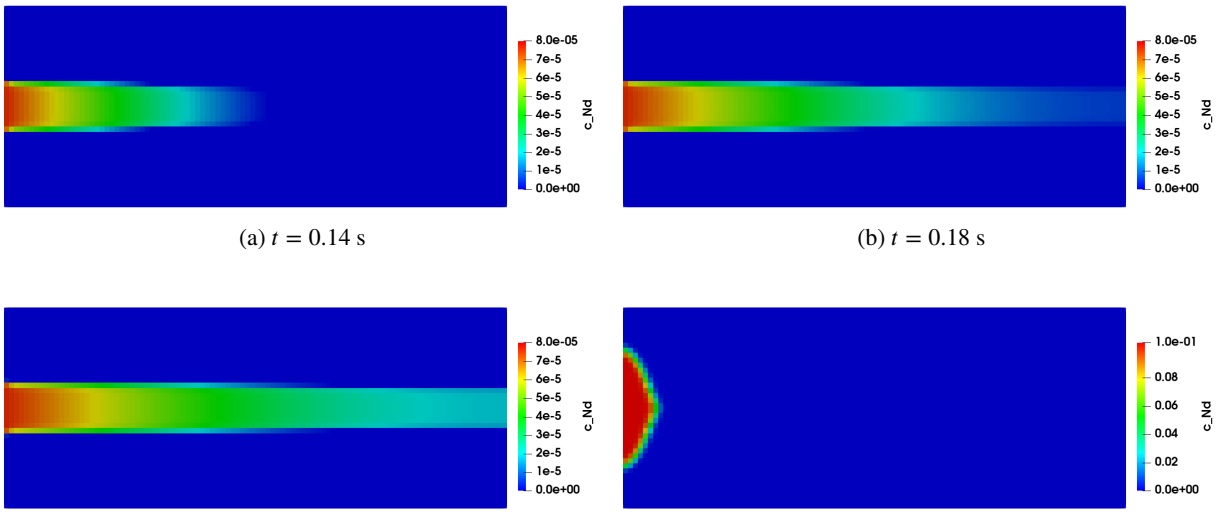

(a) $t = 0.14$ s

(b) $t = 0.18$ s

(c) $t = 0.21$ s

(d) $t = 0.38$ s

Figure 4.8. Simulations of Nd diffusion into a bicrystal, showing the evolution of c_{Nd}. In (a) – (c), a buildup of Nd along the grain boundary is shown, caused by the enhanced diffusion along the GB. (d) c_{Nd} after formation of the $Fe_{17}Nd_2$.

5. OVERALL CONCLUSIONS AND FUTURE WORK

In this report, progress in modeling cladding attack by lanthanides during FY22 was summarized. An overall strategy for implementing a mechanistic, physics-based BISON model of FCCI layer formation was described. Previous lower length scale simulations can be used to parameterize transport of lanthanides through the fuel and sodium bond layer, respectively. The work in this report studies a simplified case of diffusion of Nd through pure Fe and forms the basis for the final part of the BISON FCCI layer formation model, which considers the diffusion of lanthanides into the cladding.

Atomistic simulations were used to determine the diffusion coefficient of Nd through Fe, and to develop a parabolic approximation for the free energy of the $Fe_{17}Nd_2$ intermetallic phase. A surprising finding was that the diffusion of Nd through the intermetallic, as measured experimentally, was much faster than the diffusion through pure iron. Future atomistic simulations should be used to understand the reasons for this. In addition, future atomistic simulations should be used to determine the interfacial energy between the bcc Fe and intermetallic phases. The much more complex chemistry of the HT9 alloy compared to bcc Fe may also change the grain boundary energy; this should also be explored with atomistic simulations.

A phase-field model of the Fe-Nd system was developed and used to simulate growth of the intermetallic $Fe_{17}Nd_2$ layer in a diffusion couple experiment. The comparison of simulation results to the experimentally observed growth rate is encouraging. However, the fully formed FCCI layer has a more complex microstructure. Additional alloying elements should be added to the phase-field model and the resulting microstructures should be compared to ongoing experimental work to validate the model. The phase-field model was also used to simulate the effect of enhanced grain boundary diffusivity on $Fe_{17}Nd_2$ formation. The model did not show $Fe_{17}Nd_2$ layer formation along the grain boundary, as has been hypothesized but not definitively confirmed. If this is correct, the model may need to be reformulated to consider $Fe_{17}Nd_2$ as a grain boundary phase.

Bibliography

[1] C. Matthews et al. “Fuel-Cladding Chemical Interaction in U-Pu-Zr Metallic Fuels: A Critical Review”. In: *Nuclear Technology* 198 (1993), pp. 231–259.

[2] D. D. Keiser. *Fuel-Cladding Interaction Layers in Irradiated U-Zr and U-Pu-Zr Fuel Elements*. Tech. rep. ANL-NT-240. Argonne National Laboratory-West, 2006.

[3] J. M. Harp et al. “Scanning electron microscopy examination of a Fast Flux Test Facility irradiated U-10Zr fuel cross section clad with HT-9”. In: *Journal of Nuclear Materials* 494 (2017), pp. 227–239. DOI: 10.1016/j.jnucmat.2017.07.040.

[4] C. Jiang et al. “Bulk and surface diffusion of neodymium in alpha-uranium: Ab initio calculations and kinetic Monte Carlo simulations”. In: *J. Nucl. Mater.* 557 (2021), p. 153307.

[5] C. Jiang et al. *Determine effective diffusion coefficient of solid fission product species in metallic fuel*. Tech. rep. INL/EXT-20-60266. Idaho National Laboratory, 2020.

[6] X. Li, A. Samin, and J. Zhang. “Ab-initio molecular dynamics study of lanthanides in liquid sodium”. In: *Journal of Nuclear Materials* 484 (2017), pp. 98–102.

[7] T. L. Chen et al. “Experimental investigation and thermodynamic assessment of the Fe-Pr and Fe-Nd binary systems”. In: *Calphad* 55 (2016), pp. 270–280.

[8] T. Kajitani et al. “High-resolution neutron powder diffraction study on nitrogenated Nd_2Fe_{17}”. In: *J. Appl. Phys.* 73 (1993), pp. 6032–6034.

[9] J. P. Perdew, K. Burke, and M. Ernzerhof. “Generalized Gradient Approximation Made Simple”. In: *Phys. Rev. Lett.* 77 (1996), pp. 3865–3868.

[10] G. Kresse and J. Furthmuller. “Efficient iterative schemes for ab initio total-energy calculations using a plane-wave basis set”. In: *Phys. Rev. B* 54 (1996), pp. 11169–11186.

[11] A. Togo and I. Tanaka. “First principles phonon calculations in materials science”. In: *Scr. Mater.* 108 (2015), pp. 1–5.

[12] G. Lucas and R. Schaublin. “Vibrational contributions to the stability of point defects in bcc iron: A first-principles study”. In: *Nuclear Instruments and Methods in Physics Research Section B: Beam Interactions with Materials and Atoms* 267 (2009), pp. 3009–3012.

[13] L. Messina et al. “Exact ab initio transport coefficients in bcc Fe-X (X=Cr, Cu, Mn, Ni, P, Si) dilute alloys”. In: *Phys. Rev. B* 90 (2014), p. 104203.

[14] C. D. Versteylen, N. H. van Dijk, and M. H. F. Sluiter. “First-principles analysis of solute diffusion in dilute bcc Fe-X alloys”. In: *Phys. Rev. B* 96 (2017), p. 094105.

[15] L. Messina et al. “Systematic electronic-structure investigation of substitutional impurity diffusion and flux coupling in bcc iron”. In: *Phys. Rev. B* 93 (2016), p. 184302.

[16] G. Henkelman, B. P. Uberuaga, and H. Jonsson. “A climbing image nudged elastic band method for finding saddle points and minimum energy paths”. In: *J. Chem. Phys.* 113 (2000), p. 9901.

[17] M. Mock and K. Albe. “Diffusion of yttrium in bcc-iron studied by kinetic Monte Carlo simulations”. In: *J. Nucl. Mater.* 494 (2017), pp. 157–164.

[18] J. L. Bocquet, C. Barouh, and C. C. Fu. “Migration mechanism for oversized solutes in cubic lattices: The case of yttrium in iron”. In: *Phys. Rev. B* 95 (2017), p. 214108.

[19] H. Wu, T. Mayeshiba, and D. Morgan. “High-throughput ab-initio dilute solute diffusion database”. In: *Sci. Data* 3 (2016), p. 160054.

[20] L. K. Aagesen et al. “Grand-potential-based phase-field model for multiple phases, grains, and chemical components”. In: *Physical Review E* 98 (2018), p. 023309.

[21] G. J. Long et al. “A magnetic, neutron diffraction, and Mossbauer spectral study of the $Nd_2Fe_{17-x}Al_x$ solid solutions”. In: *Journal of Applied Physics* 76 (1994), pp. 5383–5393.

[22] N. Moelans, B. Blanpain, and P. Wollants. “Quantitative analysis of grain boundary properties in a generalized phase field model for grain growth in anisotropic systems”. In: *Phys. Rev. B* 78 (2008), p. 024113.

[23] S. Ratanaphan et al. “Grain boundary energies in body-centered cubic metals”. In: *Acta Materialia* 88 (2015), pp. 346–354.

[24] D. Zhang, I. R. McColl, and J. V. Wood. “Diffusion reactions in the iron-neodymium binary alloy system”. In: *Philosophical Magazine A* 75 (1997), pp. 959–974.

[25] J. D. Hales et al. *BISON Users Manual*. Tech. rep. INL/MIS-13-30307, Rev. 3. Idaho National Laboratory, 2015.

[26] M. Plapp. “Unified derivation of phase-field models for alloy solidification from a grand-potential functional”. In: *Physical Review E* 84.3 (2011), p. 031601. ISSN: 1539-3755. URL: <GotoISI>://WOS:000294569000002.

[27] D.A. Porter and K.E. Easterling. *Phase Transformations in Metals and Alloys*. 2nd. London: Chapman and Hall, 1992.